

Nulling Interferometry for Extra-solar Planet Detection: Sensitivity & Image Reconstruction

Thangasamy Velusamy and Charles A. Beichman
 Jet Propulsion Laboratory, California Institute of Technology
 4800 Oak Grove Dr, Pasadena, CA 91109
 818-354-6112 velu@rams.jpl.nasa.gov
 818-354-8174 Charles.A.Beichman@jpl.nasa.gov

Abstract

A typical star is more than a billion (in optical) to a million (in infrared) times brighter than the planet, making the planet undetectable in the star's glare without special efforts to suppress the starlight. Nulling interferometer suppresses starlight by pointing a null in the interference fringe pattern on the star while pointing a fringe maximum in the direction of the planet. Images of planetary systems are not formed by direct imaging, but are reconstructed after measurements have been made with the array in multiple orientations and configurations. This paper addresses the image reconstruction issues for nulling interferometer arrays and the sensitivities for planet detection. Nulling interferometers operating in 1 AU orbit with four 3.5-m telescopes can detect Earth-like planets at distances as far as 15 pc and characterize their atmospheric emission for biosignatures. Smaller versions of the nulling interferometer arrays will have the potential to study the giant planets recently detected around nearby stars.

Contents

Abstract	
3.2 Computing Output Intensity	6
4 Image reconstruction	6
4.1 OASES nulling interferometer	6
4.1.1 Cross correlation analysis	6
4.1.2 Maximum Correlation Method	7
4.2 Dual 3-element arrays	9
4.2.1 Role of chopping	9
4.2.2 6-Telescope phase shifting dual nulling interferometer	10
4.3 Spectroscopy of planetary atmosphere	13
4.3.1 Terrestrial planets	13
4.3.2 Giant planets in nearby stars	13
5 Conclusion	13
1 Introduction	
The goal of detecting and characterizing atmospheres of terrestrial planets in the habitable zones of other stars could be achieved in a number of ways. A typical star is more than a billion (in optical) to a million (in infrared) times brighter than the planet, making the planet undetectable in the star's glare without special efforts to suppress the starlight. Bracewell & MacPhie first suggested a two-element space-based infrared interferometer for planet detection, suppressing starlight by pointing a null in the interference fringe pattern on the star [1]. Using the nulling interferometry the Terrestrial Planet Finder (TPF) offers the prospect of identifying habitable and possibly even life-bearing planets orbiting other stars as far as 15 pc [2],[3]. Technical reasons such as the thousand-fold more favorable contrast ratio of the planet to star over the optical favor searching for	
1 Introduction	1
2 Nulling Interferometers	2
3 Simulating Output Data	3
3.1 Modeling the signal and noise	3
3.1.1 Source Model: Planet and Exo-zodi	3
3.1.2 Background emissions	4
3.1.3 Interferometer system contributions	4
3.1.4 Total noise calculations	4

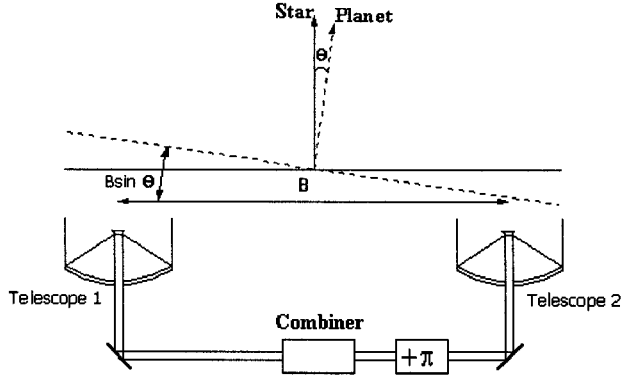


Figure 1: Concept of a two element nulling interferometer.

planets in the mid-infrared. The mid-infrared band contains numerous molecular lines from trace gasses (CO_2 , H_2O , O_3 and possibly CH_4) that can be used to assess the habitability of a planet or even to infer the presence of life itself. These lines are deep and broad and could be detectable by low-resolution spectroscopy.

TPF could be implemented in wide variety of configurations, constrained by the number of telescopes, the necessary degree of starlight and background suppression, and the required accuracy of the reconstructed images. There is a performance trade-off between the ability to provide a deep and wide null to suppress starlight combining many telescopes into a single array, and the ability to chop rapidly, to suppress large-scale diffuse emission from a zodiacal cloud by chopping between sub-arrays with relatively shallow nulls [4],[5],[6]. TPF will have the ability to optimize its performance on-orbit using a number of separate beam-combiner modules. One of the designs uses a linear array of four telescopes and can employ chopping or not depending on the configuration of the beam combiner [5],[7]. A dual 3- element nulling interferometer has also been suggested [8],[6]. This has the advantage of measuring both the amplitude and phase of the visibility, providing the necessary degree of starlight suppression and exo-zodi suppression, and the required accuracy of the reconstructed images for spectroscopy. Direct detection of extra-solar earth-like planets requires: (i) a deep and wide null to suppress the starlight, (ii) high fidelity image reconstruction capable of detecting planet emission against a bright exo-zodi, (iii) high enough sensitivity for spectroscopy. A detailed discussion of the factors affecting the sensitivity of

TPF, and nulling interferometers in general are given in [9]. In this paper we discuss the image reconstruction issues for nulling interferometer arrays and the sensitivities for planet detection.

2 Nulling Interferometers

A schematic of the first nulling interferometer proposed by Bracewell [10] is shown in Figure 1. By introducing a π phase shift in one of the interferometer beams, we can achieve destructive interference in the direction of the star while constructive interferences occur in the direction of the planet. The transmission response is given by

$$P(\theta, \alpha) \sim \sin^2 \phi \quad (1)$$

$$\phi = 2\pi \mathbf{B} \cdot \mathbf{S} / 2\lambda = (2\pi \theta B / 2\lambda) \cos(\beta - \alpha) \quad (2)$$

where \mathbf{B} is the baseline, \mathbf{S} is the line of sight of the off axis sky position (x,y) or (θ, α) . β and α are position angles of the baseline and the source, θ is the angular distance of source from the meridian plane of the interferometer. The interferometer projects a nulling interference pattern onto the sky whose depth decreases as $\sim \theta^2$.

The depth and breadth of the null required for an observation depends on the distance and radius of the star (i.e. its subtended angle). A two-element Bracewell nulling interferometer does not provide a deep enough null to suppress the star light to the desired degree. A θ^2 null does not meet the requirement that the null response be spatially broad enough to fill the stellar disk at depth $< 10^{-5}$. Several improvements to this concept of nulling interferometry have been suggested to provide broader

deeper nulls. Using more elements in the nulling interferometer provides greater starlight suppression. The null should be as broad (not to resolve the star) and deep as possible, at the same time not too broad to suppress the innermost planets. Also arrays with more than two elements have fringe patterns with more complex symmetry to help overcome ambiguities in the image reconstruction. A Mariotti nulling interferometer produces a null beam formed by combining 3 telescopes of size (1:2:1) in a linear array [4]. This provides a null response varying as θ^4 which is adequate for starlight rejection by a factor of $10^5 - 10^6$ considering the size of the stellar disk. The OASES linear array consists of 4 telescopes of sizes (1:2:2:1) [7]. This provides a broader deep null varying as θ^6 . Several other linear arrays have been suggested for TPF [11]. A 2-D array has been suggested for the European space mission DARWIN [12].

For the demonstration purposes here we adopt a 4-element nulling interferometer array [7]. The 4-element OASES interferometer is arranged in a 1:2:2:1 configuration and overall dimension B as shown in Figure 2. The interference null is achieved by combining two superposed Bracewell interferometers formed by the inner and outer two pairs. The amplitude of the outer pair is exactly half that from the inner pair and are combined with 180° phase difference. The combiner output amplitude now becomes

$$a = \sin\phi - \frac{1}{2}\sin 2\phi \quad (3)$$

The nulling pattern is given by

$$P(\theta, \alpha) = a^2 = 4\sin^2\phi\sin^4(\phi/2) \quad (4)$$

where 2ϕ is given by eq. 2. Here the null depth varies as θ^6 and that gives an exceptionally broad central minimum. A perfect interferometer would produce fringes with perfect contrast. We clip the null to have a maximum depth at 10^{-5} and 10^{-6} respectively for an interferometer located at the 1 AU and 5 AU orbits. At the closer distance, the higher local background reduces the requirements for the deepest possible null [9]. Figures 2b & c show the response pattern for two baselines.

3 Simulating Output Data

In interferometry images of planetary systems are not formed by direct imaging, but are reconstructed

after measurements have been made with the array in multiple orientations and configurations. The output from a nulling interferometer does not measure the complex visibility as traditionally the case in radio astronomy. But provides only a measure of the fringe amplitude of the planet. Besides the glare from the central star, the planet is embedded in an exo-zodiacal emission. Thus in addition to the noise, the output is also contaminated by unwanted signals such as the leakage of the star light through the null, the exo-zodi emission. The leakage of the star light through the null and the exo-zodi emission are the main sources of the photon noise in the outputs. The spectral study requires a uniform sensitivity at all wavelengths. But several factors such as the null width, spatial resolution, exo-zodi flux are wavelength dependent and affect differentially the image quality and sensitivity at different wavelengths. Thus the sensitivity of nulling interferometers (its ability to detect earth-like planets) is determined by a large wide variety of factors, some relating to the target system, some to the instrument, and some to the observing location. Therefore it is important for any feasibility study of planet detection to simulate the data carefully accounting for all possible sources of signal and noise.

3.1 Modeling the signal and noise

In order to simulate the nulling interferometer data realistically we must take into consideration all sources of both signal and noise in an observation. A variety of sources contribute to the interferometer output (see [9]).

3.1.1 Source Model: Planet and Exo-zodi

The target planet is typically taken to be an Earth-diameter blackbody at an orbital radius $a=1$ AU around a solar type star at distance $d=10$ pc. The target emission was modeled without atmosphere and with various atmospheric constituents which can modify its effective temperature at a particular wavelength.

The distribution and amount of material of the zodiacal dust in the target system is an important source of signal and noise. The exo-zodiacal cloud is extended starting at the dust melting sublimation radius and extending out to the edge of the primary beam of a single telescope. The planet emission is embedded in this extended emission from the exo-

zodi. A two-dimensional image of the zodiacal cloud is determined by integrating the 3-dimensional dust distribution for a particular inclination to the line of sight. Figures 2a shows an image of a zodiacal cloud with an embedded planet used for simulating nulling interferometer output.

For the exo-zodi model we adopt the fan-shaped form that characterizes our solar system dust, varying only the scaling factor for the optical depth to account for differing amounts of zodiacal material [13]. The temperature structure varies according to the luminosity of and distance from the central star. The spatial distribution of zodi emission at each wavelength is computed by integrating along the line of sight. The inclination of the orbital plane to the line of sight was considered while modeling exozodi-emission. A randomly fluctuating component on the scale ~ 0.1 AU at 0.5% level, and a 0.1 AU wide band emission with 1 AU radius at 10% level were added onto a smooth exo-zodi emission. Small scale structures such as blobs of size 0.1 AU to 0.5 AU were also added in some of the simulations.

Since the signal reaching the detector passes through the null pattern of the interferometer, the hot, inner portions of the zodiacal disk are hidden from view and the Poisson-noise producing zodiacal signal is decreased by about a factor of 3 from the nominal exo-zodiacal flux. Structured emission in the zodiacal light of the target star is potentially a noise source. A planet must be detected against a non-flat field of corrugations in the target field. Large, coherent structures, such as wakes and clumps behind planets, can masquerade as planets.

3.1.2 Background emissions

Local background due to dust in the solar system at the observing location also contribute to the signal in the direction of the target. The local zodiacal (LZ) cloud provides the foreground through which we must observe. The cloud is characterized by the zodiacal parameter values derived from fits to the COBE or IRAS data [13]. The LZ diminishes with distance from the Sun due to decreased dust density and decreased temperature. At short wavelengths the drop is very dramatic, (a factor of >300 at $\lambda < 7\mu\text{m}$), while at longer wavelengths the drop is less pronounced (150 at $12\mu\text{m}$).

An additional background against which we must observe is the galactic cirrus, which sets a minimum sky brightness even if there were no LZ emission [14].

A minimum value of the cirrus emission corresponding to $I_\nu(100\mu\text{m}) = 1 \text{ MJysr}^{-1}$ is included in all calculations, e.g. $I_\nu(12\mu\text{m}) \sim 0.08 \text{ MJysr}^{-1}$ from cirrus.

3.1.3 Interferometer system contributions

Additional sources of signal and noise come from interferometer system itself. The contributing factors are the size and temperature of the telescopes and associated optics, interferometer baseline and nulling configuration, pointing jitter and instrument properties such as optical efficiency, detector dark current, depth and stability of the null. The telescope and optics temperatures are set by the need to avoid any contribution to instrumental noise by the telescope. The temperature depends on the wavelength and local zodiacal foreground. At 1 AU a telescope temperature of 40 K produces $<10\%$ degradation of the sensitivity at $17\mu\text{m}$. At 5 AU, the telescope temperature must be < 35 K to avoid influencing the $17\mu\text{m}$ sensitivity. The overall system efficiency includes reflections off many optical surfaces, transmission through filters and beam splitters (0.12), detector quantum efficiency (0.5), and beam efficiency due to taking only the central part the primary beam (0.6).

The jitter in the null (wandering of the null across the star due to variations in pointing of the phase center of the interferometer) is another source of noise. Calculations show that the noise associated with this jitter is negligible for values < 1 milliarcsec. Its contribution depends on the angular diameter of the star, the breadth of the null, and the stability of the system.

3.1.4 Total noise calculations

The photon noise in the interferometer outputs were calculated as outlined in [9]. The signals from the various sources of radiation are defined in terms of photoelectrons detected by interferometer in an integration time and spectral resolution $R=20$. The total noise is the quadratic sum of all the individual components.

$$Q_{noise} = (Q_{leak} + Q_{LZ} + Q_{EZ} + RN^2 + Q_{dark} + Q_{planet} + (flat * Q_{tot})^2)^{1/2}$$

where Q represents the photoelectron counts and the suffixes indicate the various contributions. The flat field noise, $flat * Q_{tot}$, represents a systematic noise level that cannot be improved with further integration time.

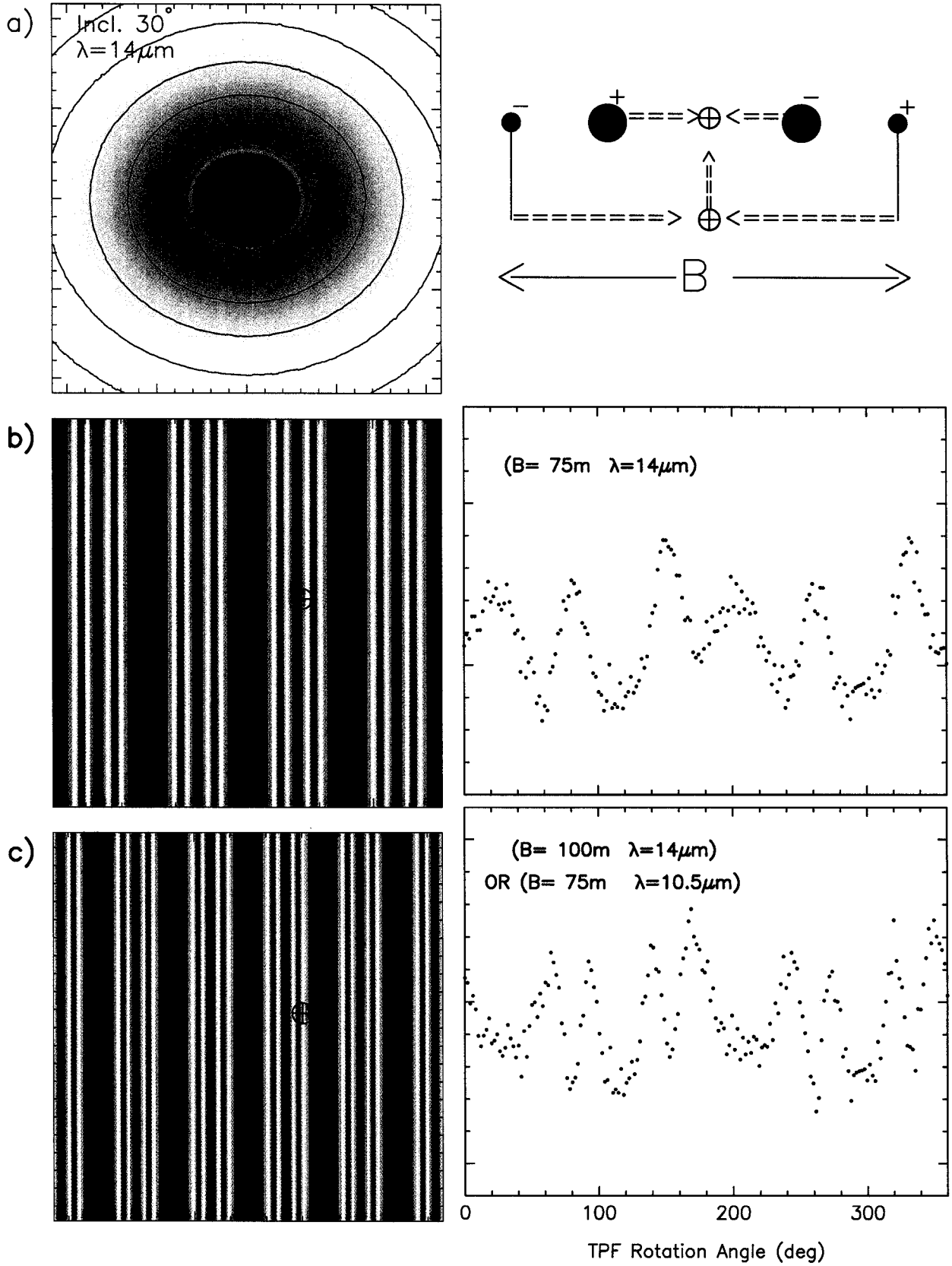


Figure 2: (a) (*left*) The model image of the exo-zodiacal emission and planet calculated for an inclination of 30° for solar type star at 10pc. (*right*) Schematic diagram of the 4-element (1.75m:3.5m:3.5m:1.75m) linear nulling interferometer. (b) & (c) (*left*) The null response patterns. (*right*) The output intensity as function of rotation angle. Note the intensity modulation caused by the planet movement in and out of the fringe maximum. The baseline and wavelengths are indicated. Total integration time 10^5 s.

3.2 Computing Output Intensity

The interferometer observable is an output intensity as a function of time as it rotates around the line of sight to the star. These data are obtained simultaneously at 20 wavelengths. The interferometer projects a nulling interference pattern onto the sky. By evaluating the two dimensional response pattern in the sky as a function of position angle we can compute the output intensity.

$$R_o(\beta, \lambda) = \sum_x \sum_y I_{mod}(x, y, \lambda) P(x, y, \beta, \lambda) \quad (5)$$

where $P(x, y, \beta, \lambda)$ is the null response at x, y pixel in the sky plane (as shown in Figures 2b & c). For I_{mod} , the source brightness (star + planet + exo-zodi) we use the images computed from the model discussed above. An example of the model brightness distribution is shown in Figure 2a. The summation is over all the pixels within the telescope beam area. The photon noise and signals from other sources as summarized above are added to R_o . For all simulations presented here we assume an interferometer in the 1 AU orbit. The results of the data simulation is shown in the right panels in Figures 2b & c. The rotation of the baseline causes the planet to move in and out of the fringe maximum in the null response. This produces a modulation in the output intensity characteristic of the fringe pattern and the planet position. In order to enhance the intensity modulation with the rotation of the interferometer, for demonstration purposes, we have used a planet radius three times that of earth (10 times more luminous than a earth).

4 Image reconstruction

The main factors that affect the fidelity of the image are the exo-zodi strength, inclination of the local ecliptic with respect to the line of sight, and structures in the exo-zodi. The u - v coverage (the number of baselines) and spatial resolution (the length of baselines) are critical factors for map fidelity. Especially the complexity of the planetary system (i.e. if several planets are present) will require a good u - v coverage. The accuracy of the planet flux measurement will also depend on the degree of uniformity of the null response across the field of view. The spectral study requires a uniform performance at all wavelengths. But several factors such as the

null width, spatial resolution, exo-zodi flux are wavelength dependent and affect differentially the image quality and sensitivity at different wavelengths. Planet detection alone can be relatively easy because data at all wavelengths can be combined to produce a single image. This is equivalent to using several baselines to provide measurements over a wider range of spatial frequencies (u - v). But, the characterization of the planet by its spectrum in the 7 to 20 μ m region requires a capability for accurate measurements of planet flux density at each wavelength. The detection of the planet requires achieving a high contrast by spatially filtering out some of the large scale features in the exo-zodi.

In interferometry the images are not formed directly and only an indirect image can be produced using the observed data. The Fourier transform technique is commonly used in all radio interferometers. This is not possible in general for the nulling interferometers because they do not measure the complex visibility. But they provide only a measure of the fringe amplitude of the planet. Only in some special cases, a dual nulling interferometer configurations can provide the complex visibility to make use of the simple Fourier transform technique (see section 4.2.2). Nulling interferometers such as the OASES four telescope array produce an output which shows intensity modulation with the rotation of the baseline (Figure 2). This data stream can be turned into an image using some of the numerical techniques such as Maximum Entropy, CLEAN. We have used the Maximum Correlation Method (MCM) used in the high resolution image reconstruction of IRAS data [15]. We have adopted the tools and techniques that have been developed at IPAC for HIRES (HIGH-RESolution) image construction program [16]. We used MCM in the our simulations for OASES nulling interferometer in two configurations without chopping (section 4.1) and with chopping (section 4.2.1) and Fourier transform technique for the 6-telescope phase shifting dual nulling interferometer (section 4.2.2).

4.1 OASES nulling interferometer

4.1.1 Cross correlation analysis

As discussed in section 3.2, the interferometer output intensity at position angle β of the baseline at

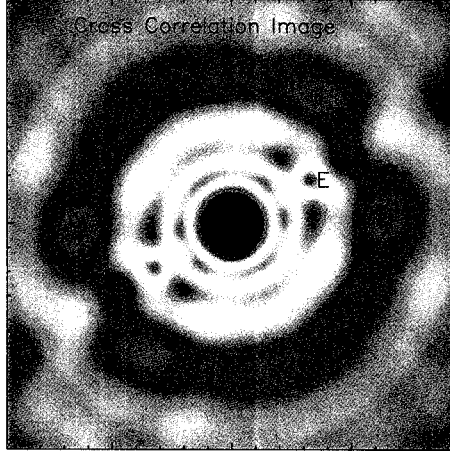


Figure 3: Cross correlation analysis image reconstruction of an Earth-like planet. The data simulated for OASES 4- telescope nulling interferometer with baseline 75m for 1Z (Solar-zodi) at inclination 0° . Data at all wavelengths 7 - 17 μm were used.

wavelength λ , $R_o(\beta, \lambda)$ is given by,

$$R_o(\beta, \lambda) = \sum_x \sum_y I(x, y, \lambda) P(x, y, \beta, \lambda) \quad (6)$$

We can invert equation 6 by taking the cross correlation [7],[17],

$$I(x, y) = \sum_\beta \sum_\lambda R_o(\beta, \lambda) P(x, y, \beta, \lambda) \quad (7)$$

The summation is over all the rotation angles and wavelengths. The summation over all wavelengths gives a mean brightness with higher sensitivity, which is useful for planet detection. Figure 3 shows an example of the image reconstructed by the cross correlation analysis. Data similar to that shown in Figure 2, but obtained for a planet with 1 Earth radius and 75m baseline, at all wavelengths 7 - 17 μm , were used for this image reconstruction. This certainly provides a useful first order image of the planet. However, it is not very useful to obtain the spectrum of the planet, as it combines the data at all wavelengths. In principle we could compute $I(x, y, \lambda)$ by summing over only the rotation angle at each wavelength (eq. 7). But this does not yield good images unless we use data from multiple baselines. Our simulations show that the MCM approach offers better reconstruction at each wavelength.

4.1.2 Maximum Correlation Method

MCM reconstructs the image recursively, starting with an initial image uniformly sampled in a rectangular grid in the image space. MCM constructs the

image in such a way that maintains the maximum pixel correlation consistent with the measurements and the null response pattern.

$$I_0(x, y, \lambda) = 1 \quad (8)$$

The first iteration computes the interferometer output by summing over the pixel brightness in this initial image modified by the response pattern of the null at wavelength λ ,

$$R_c(\beta, \lambda) = \sum_x \sum_y I_0(x, y, \lambda) P(x, y, \beta, \lambda) \quad (9)$$

A correction factor $c(x, y, \beta, \lambda)$ for each pixel is obtained by comparing the measured intensity with that computed in the current iteration $R_c(\beta, \lambda)$.

$$c(x, y, \beta, \lambda) = \frac{R_o(\beta, \lambda)}{R_c(\beta, \lambda)} P(x, y, \beta, \lambda) \quad (10)$$

A mean correction factor $c_{av}(x, y, \lambda)$ is obtained from the above ratio for all rotation angles at each wavelength. This correction is applied to obtain an improved estimate of the pixel brightness.

$$I_1(x, y, \lambda) = c_{av}(x, y, \lambda) I_0(x, y, \lambda) \quad (11)$$

This procedure is continued for few iterations (~ 40) till convergence is achieved (i.e. $c_{av}(x, y, \lambda)$ is unity).

If we are interested in just imaging the planet (for detection only) we can average over all observed wavelength at each iteration. In eq. 11 we will use $c_{av}(x, y)$ which is averaged over all wavelength instead $c_{av}(x, y, \lambda)$ and replacing $I(x, y, \lambda)$ by $I(x, y)$ in

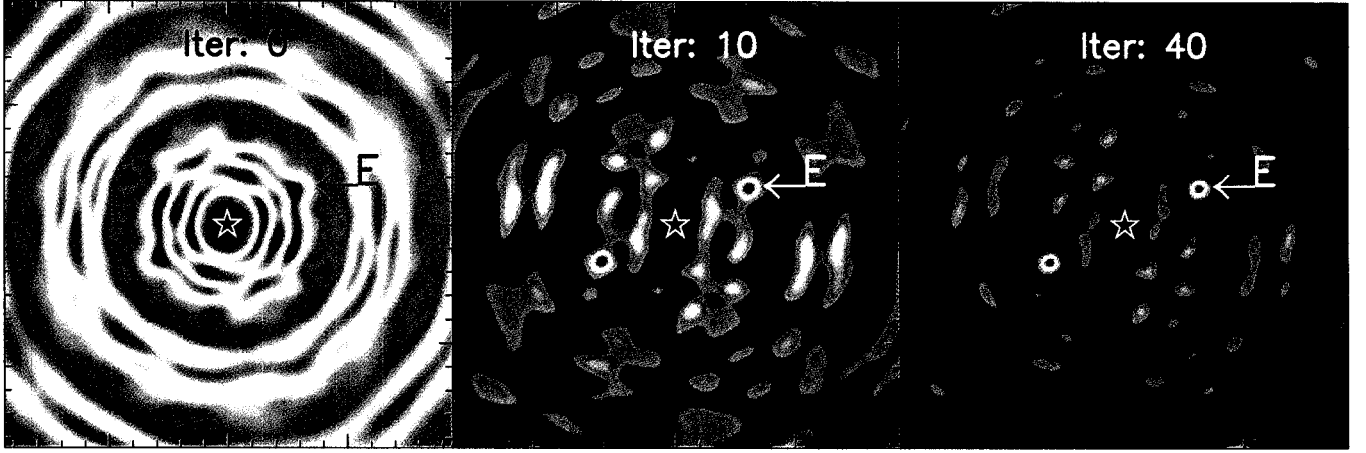


Figure 4: Image reconstruction by the MCM algorithm using the interferometer output data shown in Figure 2b at $14\ \mu\text{m}$. The panels show images at 1, 10 and 40 iterations.

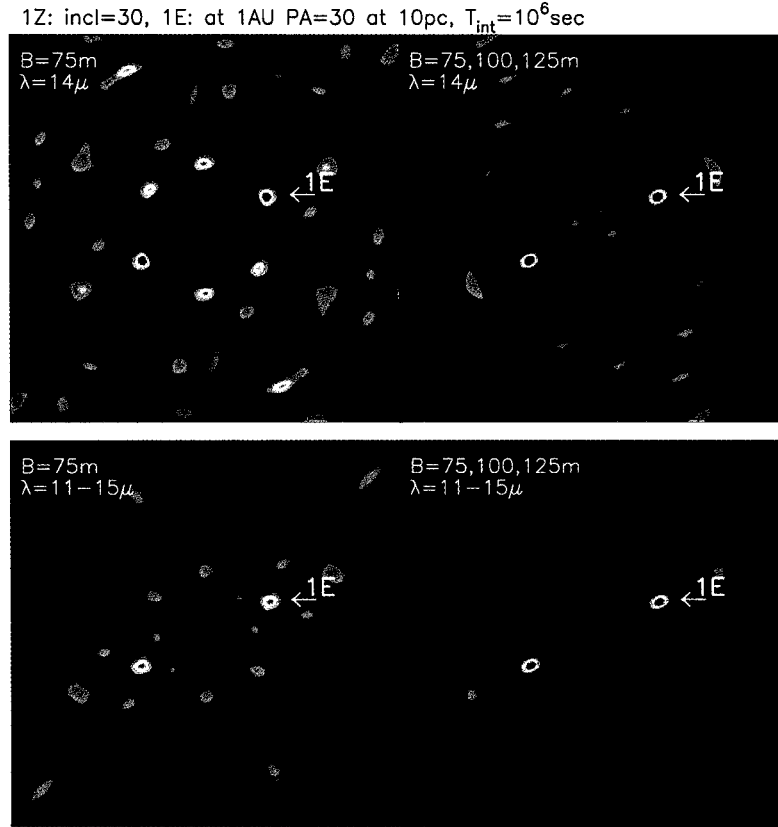


Figure 5: Imaging an earth at 10 pc using a 4-element nulling array by combining baselines and wavelengths. The panels show images obtained at one wavelength using one or multiple baselines and images obtained using all wavelengths in one or multiple baselines.

all the equations above. The same algorithm works when we have multiple baselines. Appropriate response pattern for each baseline data is used in eq. 9 & 10 and the mean correction factor $c_{av}(x, y, \lambda)$ is obtained by summing over the rotation angles for all baselines. Figure 4 shows the results of the image reconstruction as outlined above, carried out using the simulated interferometer data shown in Figure 2. The MCM reconstruction used output intensities measured in 180 position angles of a single baseline (100m) at one wavelength (14 μm). The images obtained at iteration 1, 10 and 40 are shown. These images show good convergence after 10 iterations. In order to demonstrate the techniques we have used a brighter target for the planet observed in one baseline and wavelength with shorter integration. However this approach provides desirable results for a typical Earth-like planet as shown in Figure 5. The images in Figure 5 also demonstrate that combining wavelengths and/or baselines greatly enhances the planet's image. Some of the extended features in the reconstructed images are the result of the extended exo-zodi emission in the planetary system. A spatial filtering on the scale of a few resolution element also helps to enhance the brightness of the planet in the images.

The interferometer output signals (Figure 2a & b) are symmetric about a 180° rotation of the baseline. This results in the planet appearing twice reflected through the central star in the images shown Figures 3 - 5. This can be removed with more sophisticated data acquisition (chopping) and image processing strategies.

4.2 Dual 3-element arrays

One of the limitations of the OASES 4-element array is that it does not resolve out the extended exo-zodi emission. The reconstructed images shown in Figure 5 represent an exo-zodi system in which the ecliptic is inclined at 30° to the plane of the sky. However it becomes increasingly difficult to image systems with larger inclination. In the face on case the exo-zodi is circularly symmetric and therefore does not introduce any modulating signal with rotation of the baseline. However at higher inclination the exo-zodi brightness distribution is elongated with major axis at the position angle of its ecliptic. This introduces an intensity modulation in addition to that by the planet. Filtering out the zodiacal modulation helps to some extent in the image reconstruction, but at

the expense of losing some of the planet signal. Dual linear nulling arrays in which pairs of nulling interferometers are combined in various ways are useful in rejecting unwanted noise and signals (exo-zodi). Several such configurations have been suggested [11].

4.2.1 Role of chopping

We consider a OASES 4-element array which can also be configured as a dual 3-element array [8],[18]. Figure 6 shows a schematic diagram. The inner two telescopes with larger diameter are shared to form an interferometer pair as indicated in the figure. Each element (a Mariotti nulling interferometer) produces a null beam formed by combining 3 telescopes of size (1:2:1) in a linear array. The two null beams are combined as in a two-element interferometer. Chopping is achieved by switching a variable phase shift Φ in one of the null beams. Chopping between phase shifts $\Phi = 0$, and $\Phi = \pi$ produces a Cos-chop output. Similarly a Sine-chop output is produced by chopping between phase shift $\Phi = \pi/2$, and $\Phi = 3\pi/4$. The chopped null response pattern are shown in Figure 6 along with that of 4-element array without any chopping. The results of our simulations for earth-like planet and exo-zodi inclination of 30° are shown in Figure 6 for these cases. As may be expected from the null response patterns there is little difference between the Cos-chop and the case without chopping. Both images are heavily contaminated by the exo-zodi emission and the planet is barely detectable. On the other hand the Sin-chop which has a response pattern asymmetrical about the central star resolves out the more extended exo-zodi brightness. As a result the planet is seen with greater contrast. Also a positive image of the planet appears at the correct location. We modified the MCM image reconstruction slightly for the Sin-chop data because in this case the output value becomes zero and negative at some rotation angles. (With no chopping or Cos-chop the output is always > 0 .) Therefore we define the correction as difference between the computed and observed outputs. Replace eq. 10 by,

$$c(x, y, \beta, \lambda) = (R_o(\beta, \lambda) - R_c(\beta, \lambda))P(x, y, \beta, \lambda) \quad (12)$$

this correction is added to the value in the image pixel instead of multiplying as in eq. 11. A negative image of the planet appearing in the opposite location, is an artifact resulting from the reconstruction algorithm. A negative brightness at the neg-

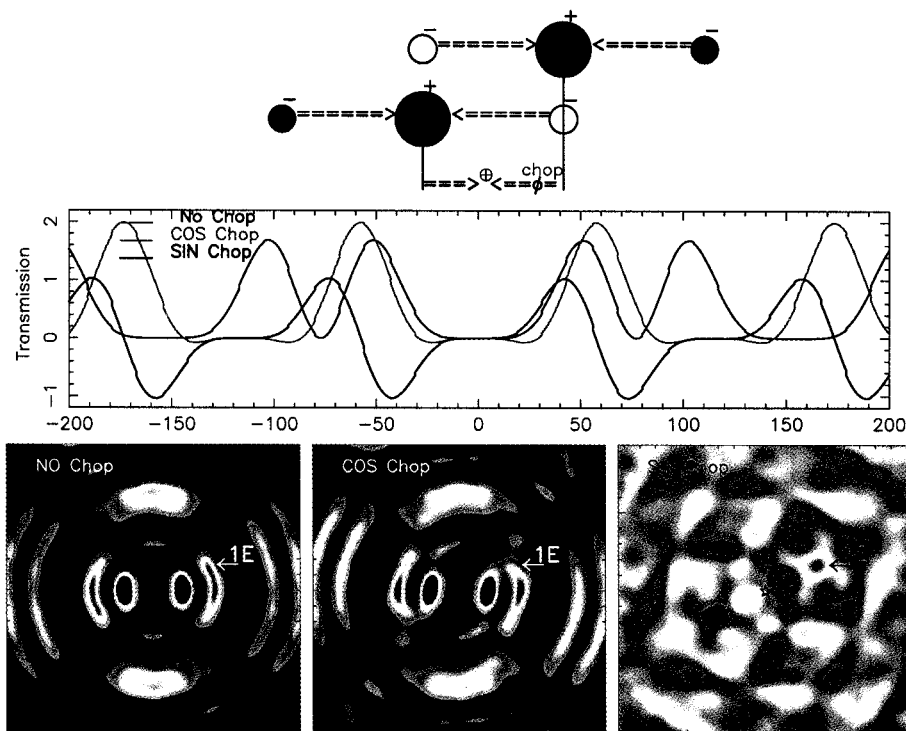


Figure 6: (a) A schematic showing dual nulling interferometer with two shared elements. (b) Null response pattern for Cos/Sine chop. The no chopping case represents that for a OASES 4-element array. (c) The corresponding images at $\lambda = 14 \mu\text{m}$. The overall baseline is 90m; 3-element nulling baseline is 60m.

ative response of the null pattern also produces a positive signal which is indistinguishable from that at the real position. Our simulations demonstrate Sine-chop greatly enhances the imaging potential of a nulling interferometer array.

4.2.2 6-Telescope phase shifting dual nulling interferometer

It is possible to take much greater advantage of the chopping if we can have a 6-telescope linear array as discussed in [6]. The basic design is that of a phase shifting two element interferometer. The elements themselves are nulling interferometers. Figure 7 shows a schematic sketch of the 6-telescope configuration. Each element (a Mariotti nulling interferometer) produces a null beam formed by combining 3 telescopes of size (1:2:1) in a linear array. Because there is no sharing of the telescope as in the case of 4-elements discussed in the previous section, the length of baselines for the 3-telescope nulling elements and that between them can be chosen independently. The baseline of each nulling element b is \sim of 30 - 50m, while the separation between them can be large, baseline $B \sim 100$ - 1000 m. The nulling

elements can be flown on two separate free flyers and the chopper and beam combiners on a third free flyer as indicated in Figure 7a. Because the baselines b , and B are independent, the null response characteristics (determined by b) and spatial resolution (determined by B) are totally de-coupled. This is a big advantage because in other configurations, increasing the baseline to achieve higher spatial resolution would lead to a narrower null which will result in less starlight suppression, by resolving the central star. Besides, that $B \gg b$ makes the imaging much easier and identical to that in radio interferometry. In Figure 7c are shown the null response patterns of the Cos and Sin chop for $b=40\text{m}$ and $B=150\text{m}$. The response pattern of the sin-chop is asymmetrical about the central null while that of the cos-chop is symmetrical. Unlike the case of the chopping in 4-element array (Figure 6) now both Sin- and Cos- chops show sinusoidally varying response patterns, reminiscent of the sin and cos correlator outputs of an radio interferometer. Thus the chopped output responses represent a sine and cosine fringe pattern in the image plane (x,y). Therefore, cos/sin chop output may be regarded as a measure the real and imaginary quantities of the complex visibility at the u-v corre-

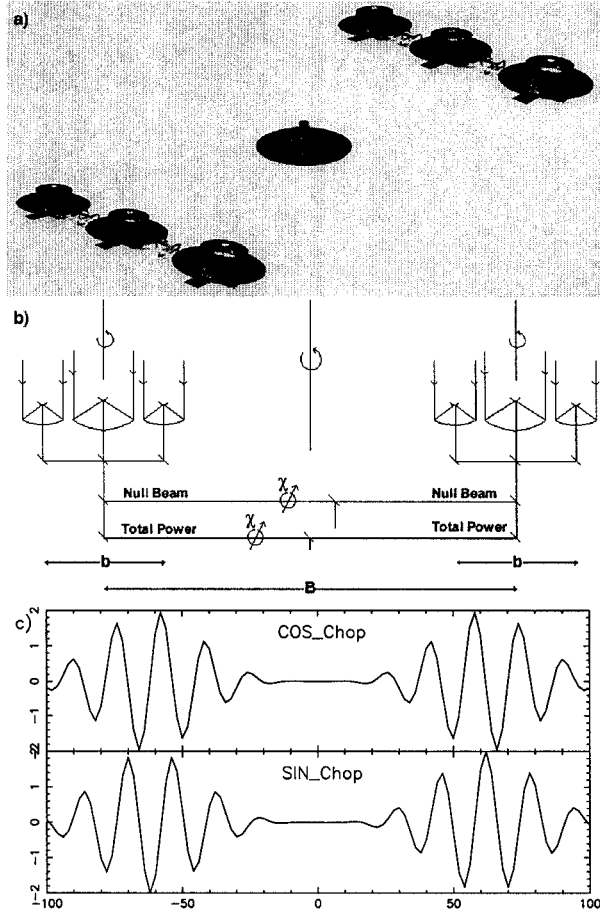


Figure 7: (a) An artist sketch of 6-telescope TPF. (b) A schematic of the nulling interferometers and the combiner for the null beams. A chopped output is obtained by Switching a variable phase shift χ in one of the null beams. The total-power beams are also indicated for general use in astrophysics. (c) The sine/cosine chop responses for baseline $B=150\text{m}$ and $b=40\text{m}$ at $12\mu\text{m}$.

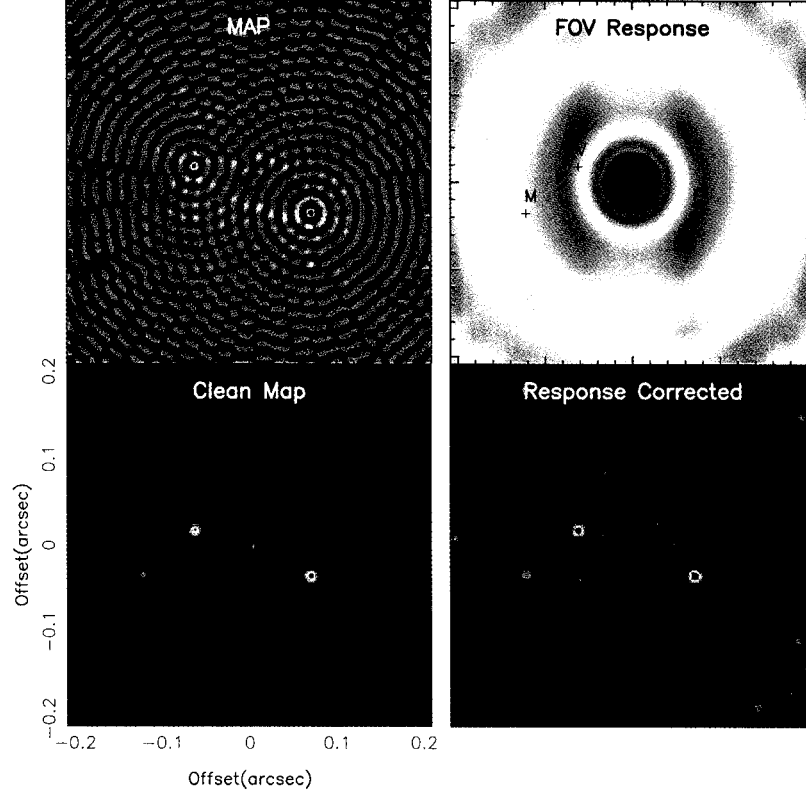


Figure 8: Imaging a solar system analog with Earth, Mars and Venus at 10 pc. The simulated complex visibilities sampled by rotating the TPF baselines were used: $\lambda = 14 \mu\text{m}$ and baselines $b=30\text{m}$, $B=150\text{m}$. In the gray scale images the highest intensities are represented by the darkest area.

sponding to the length and orientation of baseline **B**. Although the sin/cos chop responses are not entirely sinusoidal (as their amplitudes are attenuated at the fringe minimum of the 3-element null response), the planets being point objects the fringes are sinusoidal locally, and we can treat their outputs as a measure of a complex visibility. Different u-v points can be sampled by rotating the baseline **B**, while keeping the nulling baseline **b** fixed. The image $I(x,y)$ of the brightness around the star is obtained by Fourier transforming the complex visibilities measured at a number of u-v points. The brightness of the planet in the reconstructed image will correspond to the true brightness reduced by the 3-telescope null response pattern.

Figure 8 shows an example of this approach for imaging a solar system analog with Mars, Venus and Earth at a distance of 10 pc. The 3-telescope null responses act like a primary beam in a 2- element interferometer. Rotating the null baseline through 0° to 180° enables that each planet is observed near the maximum in the null response at least in a few

orientations. This allows a fairly uniform sensitivity for planet detection within the field of view, for each u-v measurement (see Figure 8). For the complex visibility at each u-v point sampled, we could use the average values measured by rotating the nulling elements. To obtain the true flux of the planets, the cleaned map is corrected for the average null response, $\langle P(x,y) \rangle$, as shown in Figure 8.

It may be noted that the image shown in Figure 8 is for the case of a high inclination of the exo-zodi, at 60° . This result is a very significant improvement over the other configurations in which the large axial ratio in the exo-zodi for high inclinations, introduces a correspondingly large modulation in their output with rotation of the baseline. This inhibits planet detection. The exo-zodi effects are significantly reduced in the present configuration because of the sinusoidal fringe responses of the interferometer (Figure 7c) help resolving out the exo-zodi emission. Our simulations also indicate that for the 1Z cases the u-v sampling with a single baseline $B > 100\text{m}$ is adequate to image a three planets system. This is

possible because the planets are point sources and the exo-zodi is resolved out. However, in the case of strong exo-zodi $\sim 10\times$ longer baselines ≥ 300 m are required to detect Earth-like planets.

A 6-telescope dual nulling interferometer offers a spectacular combination of high spatial resolution and sensitivity for general purpose astrophysical imaging as well. In principle the six-telescope configuration with appropriate beam combiners and a switch yard allows simultaneously 7 independent baselines. Even in its simplest form (Figure 7) the visibilities measured by the total power beams alone would be adequate for imaging compact structures. The total-power responses of each nulling interferometer act only as a primary beam of a two-element interferometer as discussed above.

4.3 Spectroscopy of planetary atmosphere

4.3.1 Terrestrial planets

To study the spectral capabilities the nulling interferometers, the flux densities at each wavelength were measured from the simulated maps for Earth with and without atmosphere. To simulate the data we used the 6-telescope dual nulling interferometer with 150m overall baseline and 30m baseline for the 3-telescope nulling. As shown earlier in Figure 8, a moderate single baseline of ~ 150 m provides the fidelity required to image the planet using just in one wavelength data. The images were reconstructed at each wavelength and the flux densities of the planet were measured from the maps. In Figure 9 we plot the flux densities as measured from the maps and compare them with the black body spectrum for Earth. Our results indicate that the CO_2 , H_2O , and O_3 bands are detectable with similar interferometer configuration, observing and imaging strategies.

4.3.2 Giant planets in nearby stars

More than 50 extra-solar giant planets are known to date by the radial velocity techniques (reported by G.W Macy at the Manchester IAU meeting). These have masses that range for a Saturn mass up to a few Jupiter masses. They are located much closer to the parent stars at distances of < 0.1 AU to < 3 AU. Observationally almost nothing is known about their physical and chemical atmospheric properties. The nongray model calculations of the atmospheres

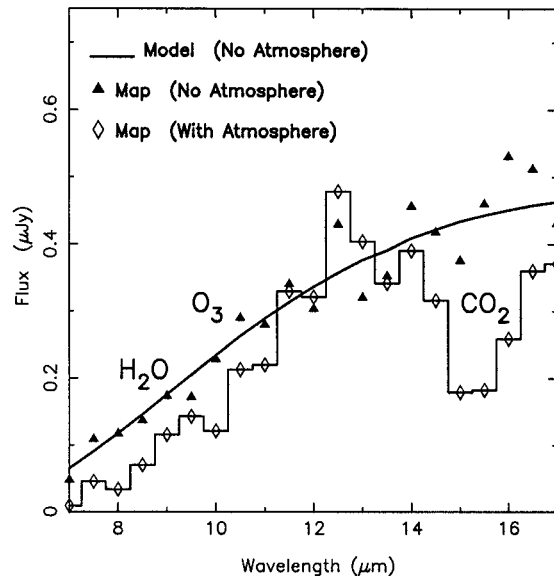


Figure 9: Example of a simulated TPF spectrum of a Earth-like planet at 10 pc. The black body spectrum (no atmosphere) is indicated by the solid line. The symbols (filled triangle and diamond) represent the fluxes measured at each wavelength from the simulated TPF images. The simulated data corresponds to a dual 3-element nulling interferometer (overall baseline 150m) and 200 hours of integration using 3.5m telescopes. Note that the atmospheric features are clearly visible in the simulated spectrum.

of extra-solar giant planets indicate effective temperatures in the range of 500K to 300K for distances 0.5 AU to 2.5 AU [19]. Thus the nulling interferometry provides an excellent tool to study their properties in the near- and mid- IR wavelengths. Further a Jupiter at same distance from the Sun as Earth would be more than 100 times brighter than the Earth simply because of the larger radius. Preliminary studies following the strategies discussed here for terrestrial planets, indicate that an opportunity exists for a near term mission using < 1 m class size telescopes and short baseline on 50 to 60m boom. Feasibility exists for spectral studies of these planetary atmospheres in several species such as CH_4 with moderate spectral resolution of ~ 100 .

5 Conclusion

The results of our simulations illustrate the technical feasibility for detecting Earth like planets: warm, with water and an oxygen-containing atmosphere, in nearby stars by using the nulling interferometry.

We have developed strategies for simulating and processing nulling interferometer data. We show that the Maximum Correlation Method is a very useful tool for imaging planets from the intensity modulation of interferometer data with the rotation. Phase chopping is essential to mitigate the exo-zodi problem and greatly enhances prospects of planet detection. Dual nulling interferometers have definite advantage over the others as they provide chopping. Especially the 6-telescope dual nulling interferometer measures both visibility amplitude and phase. It provides a straight forward synthesis imaging using the complex Fourier transform of the visibilities. It allows freedom to select a shorter baseline for the 3-telescope nulling and a much longer overall baseline. There is no performance trade off between the ability to provide deep and wide null to suppress starlight and the ability for high spatial resolution. This also has the potential to serve as an observatory for general astrophysical interests. In the long range TPF using 3.5m telescopes will be able to find planets around neighboring stars that are like the Earth in a few hours and obtain their atmospheric constituents in few hundred hours. In the near future a nulling interferometer using smaller $< 1\text{m}$ telescopes on short baselines $< 60\text{m}$ will have the potential to study the extra-solar giant planets in the nearby stars. The simulations presented in this paper provide a useful tool to evaluate performance of future planet finding missions.

Acknowledgments

We thank John Fowler at IPAC for helping us with the MCM algorithm. Our special thanks to Harman Smith and Shankar Velusamy for the art work in Figure 7. This research was conducted at the Jet Propulsion Laboratory, California Institute of Technology, under contract with NASA.

References

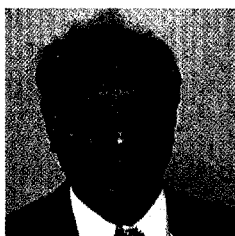
- [1] R.N. Bracewell and R.H. McPhie, "Detecting Nonsolar Planets", *Icarus* 38, 136, 1979.
- [2] C. A. Beichman, ed. *A Road Map for the Exploration of Neighboring Planetary Systems (The Ex-NPS Report)*, (JPL: Pasadena), JPL 96-22,1996.
- [3] C.A. Beichman, N. J. Woolf, and C.A. Lindensmith, Eds. *The Terrestrial Planet Finder*, (JPL: Pasadena), JPL 99-3,1999.
- [4] J-M. Mariotti and B. Mennesson, *Internal ESA Report for IRSI Project*, 1997.
- [5] N.J. Woolf et al. "Planet Discoverer Interferometer (PDI) I: A Potential Precursor to Terrestrial Planet Finder", *Proc. SPIE 3350, Astronomical Interferometry*, ed. R.D Reasonberg 683, 1998
- [6] T. Velusamy, C.A. Beichman and M. Shao, "A Dual 3-Element Nulling Interferometer for TPF", *Optical and IR Interferometry from Ground and Space*. S.C.Unwin, and R.V. Stachnick, eds. ASP Conference Series Vol.194 (San Francisco: ASP), 427, 1999.
- [7] J.R.P. Angel and N.J. Woolf, "An Imaging Nulling Interferometer to Study Extrasolar Planets", *Astrophys. J*, 475, 373, 1997.
- [8] M. Shao, *A Road Map for the Exploration of Neighboring Planetary Systems (Ex-NPS Report)*, ed. C.A. Beichman, (JPL: Pasadena), JPL 96-22,1996.
- [9] C.A. Beichman, and T. Velusamy, "Sensitivity of TPF Interferometer for Planet Detection", *Optical and IR Interferometry from Ground and Space*. S.C.Unwin, and R.V. Stachnick, eds. ASP Conference Series Vol.194 (San Francisco: ASP), 405, 1999.
- [10] R.N. Bracewell, "Detecting Nonsolar Planets by Spinning Infrared Interferometer", *Nature*, 274,780, 1978.
- [11] P.R. Lawson, P.J. Dutmount and M.M. Colavita, "Interferometer Designs for the Terrestrial Planet Finder", *Optical and IR Interferometry from Ground and Space*. S.C.Unwin, and R.V. Stachnick, eds. ASP Conference Series Vol.194 (San Francisco: ASP), 423, 1999.
- [12] Leger et al. "The DARWIN Project" *Astrophys. & Space Sc.* 241,135, 1996.
- [13] Reach et al. "Observational Confirmation of a Circumsolar Dust Ring by the COBE Satellite", *Nature*, 374, 521, 1995.

- [14] J.P. Bernard et al. "Modeling of IR emission of interstellar clouds. I - Emission of isolated clouds and dust abundance variations", *Astron. Astrophys*, 263,258, 1992.
- [15] H.H. Aumann, J.W. Fowler and M. Melnyk, "A Maximum Correlation Method For Image Construction of IRAS Survey Data", *Astron. J.* 99, 1674, May, 1990.
- [16] J.W. Fowler and H.H. Aumann, "HIRES and Beyond", *Science with High Resolution Far Infrared Data*, eds. S. Terebey, and J. Mazzaralla, (JPL: Pasadena), 1994.
- [17] R.H. McPhie and R.N. Bracewell, *NASA Report Interchange*, NCA2-OR745-716, 1978
- [18] N.J. Woolf and R.P.J. Angel, "Planet Finder Options I: New Linear Nulling Array Configurations", *Planets Beyond the Solar System and the Next Generation of Space Missions*, ASP Conference Series, ed. David Soderblom, p285, 1997.
- [19] A. Burrows et al., "A Nongray Theory of Extrasolar Giant Planets and Brown Dwarfs", *Astrophys. J.*, 491, 856, December, 1997.

has a Ph.D. in astronomy from the University of Maryland.



Chas Beichman is the chief scientist for NASA's *Origins Program* at the *Jet Propulsion Laboratory*. Previously, he was the *Director of the Infrared Processing and Analysis Center (IPAC)* at *Caltech*. His astronomical research includes the study of brown dwarfs and the formation of solar type stars. He is currently the project scientist for the *TPF mission*. He received his undergraduate degree in astronomy from *Harvard College* and his graduate degrees from the *University of Hawaii*.



Thangasamy Velusamy (Velu) is the team lead for *Radio and Submillimeter Astronomy* in the *Jet Propulsion Laboratory*. Previously, he served as the *Director of the Ooty Radio Observatory*, in *India*. Besides his interests in *interferometry* and *image processing*, his astronomical research includes the study of *star formation*, *supernova remnants* and *interstellar medium*. He is a member of the *Space Interferometry Mission (SIM) Science Planning Team* and is also a member of the *TPF Study Team*. He